Remote Sensing of Environment 141 (2014) 231–242

Contents lists available at ScienceDirect

Remote Sensing of Environment

journal homepage: www.elsevier.com/locate/rse

Wetland inundation mapping and change monitoring using Landsat and airborne LiDAR data

Chengquan Huang [a], Yi Peng [a], Megan Lang [b], In-Young Yeo [a,*], Greg McCarty [c]

[a] Department of Geographical Sciences, University of Maryland, College Park, MD 20742, USA
[b] USDA Forest Service Northern Research Station, Beltsville, MD 20705, USA
[c] USDA-ARS, Remote Sensing and Hydrology Laboratory, Beltsville Agricultural Research Center, Beltsville, MD 20705, USA

ARTICLE INFO

Article history:
Received 17 May 2013
Received in revised form 5 September 2013
Accepted 16 October 2013
Available online xxxx

Keywords:
Forested wetlands
Subpixel inundation percentage (SIP)
Change
Landsat
LiDAR

ABSTRACT

This paper presents a new approach for mapping wetland inundation change using Landsat and LiDAR intensity data. In this approach, LiDAR data were used to derive highly accurate reference subpixel inundation percentage (SIP) maps at the 30-m resolution. The reference SIP maps were then used to establish statistical relationships between SIP and Landsat data. Inundation changes were mapped by applying the derived relationships to Landsat images acquired in different years. This approach was applied to the upper Choptank River sub-watershed to map wetland inundation for average (2005 and 2007), dry (2009), and wet (2010) years. The derived SIP maps revealed large changes in wetland inundation among dry, average, and wet years. Total areas of near complete inundation (SIP > 75%) and high inundation (SIP between 50% and 75%) in the wet year of 2010 were about five and three times of those in the dry year of 2009, respectively. The wet year also had more medium inundated areas (SIP between 25% and 50%) than the average and dry years, but low inundated areas (SIP < 25%) did not have any particular trend. The mapped inundation changes were found correlated with local drought conditions and stream flow, with the near complete inundated and highly inundated areas having the highest correlations. Given the fact that Landsat are globally available and LiDAR data are becoming increasingly more affordable and available, the approach developed in this study has potential for deriving historical inundation changes over the past decades and for monitoring ongoing changes over much larger areas than demonstrated in this study.

© 2013 Elsevier Inc. All rights reserved.

1. Introduction

Wetlands provide a broad range of ecosystem services, including flood control, sediment and nutrient retention and export, water purification, groundwater replenishment, and rich biodiversity (Groot, Stuip, Finlayson, & Davidson, 2009). The provision of these services is especially vital in the Chesapeake Bay Watershed, which drains to one of the largest and historically most productive estuaries in the U.S. Effective wetland conservation and management requires reliable and up-to-date wetland information. National wetland products have been produced by the U.S. Fish and Wildlife Service (FWS) National Wetland Inventory (NWI) (Wilen & Bates, 1995) and the National Oceanic and Atmospheric Administration (NOAA) Coastal Change Analysis Program (C-CAP) (Klemas, Dobson, Ferguson, & Haddad, 1993). The NWI products provide relatively fine-scale details, but they are often out of date and contain significant errors, especially in difficult-to-map areas like forested wetlands (Kudray & Gale, 2000; Stolt & Baker, 1995). C-CAP maps are more recent but are less reliable than NWI over forested wetlands. Neither of these maps provides adequate information on the temporal dynamics of wetland inundation and saturation.

Most wetlands in the Mid-Atlantic region have certain levels of deciduous forest cover (Lang & Kasischke, 2008). Their water levels can have substantial seasonal variations, primarily in response to precipitation events and changes in evapotranspiration. Many wetland areas are inundated or saturated for a relatively short period, usually in the spring after snowmelt and before leaf-out. Inter-annual deviations from average weather conditions modify these seasonal hydrologic patterns (Mitsch & Gosselink, 2007; Tiner, 1999), such that area inundated in the spring can vary considerably during dry and wet years. Such temporal variations may further increase as rising temperatures and more variable precipitation patterns are predicted for the Chesapeake Bay region (Fisher, 2000; Moore & Kim, 1995). Because wetland inundation and saturation are the most important abiotic factors controlling wetland extent and function (Nestler & Long, 1997), even small changes in hydrologic regime may cause substantial changes in ecosystem characteristics and function (Mitsch & Gosselink, 2007). Therefore, monitoring the inundation dynamics of wetlands is critically important for understanding their health and function, and the ecosystem services they provide.

* Corresponding author.

0034-4257/$ – see front matter © 2013 Elsevier Inc. All rights reserved.
http://dx.doi.org/10.1016/j.rse.2013.10.020

Remote sensing provides a major data source for monitoring wetland dynamics. While imaging radar has been found useful for mapping wetland inundation (e.g. Lang & Kasischke, 2008; Lang, Kasischke, Prince, & Pittman, 2008) and detecting water level change in swamp forests (Lu et al., 2005), in this study we focus on the usefulness of Landsat data for monitoring inundation changes over forested wetlands. Created by a series of seven Landsat systems (Green, 2006), including the Landsat Data Continuity Mission (or Landsat 8) that was successfully launched in 2013, the Landsat archive provides a consistent imagery record of the Earth's surface that extends back to the 1970s (Goward et al., 2006) and will be continued for the foreseeable future (Loveland & Dwyer, 2012). Radar cannot provide such a consistent record over multiple decades. Existing radar data were acquired with different wavelengths, polarizations, and incidence angle ranges (Lang & Kasischke, 2008), and did not become available until the 1990s (Kramer, 2002).

Landsat data have been used in many wetland studies (e.g. Lunetta & Balogh, 1999; Thomas, Kingsford, Lu, & Hunter, 2011), including wetland classification (e.g. Berberoglu, Yilmaz, & Ozkan, 2004; Castaneda & Ducrot, 2009) and change detection (e.g. Baker, Lawrence, Montagne, & Patten, 2007; Kassawmar, Rao, & Abraha, 2011; Nielsen, Prince, & Koeln, 2008). Comprehensive reviews of remote sensing datasets and methods for wetland characterization have been provided by Rundquist, Narumalani, and Narayanan (2001) and Ozesmi and Bauer (2002). Overall, previous studies have demonstrated the potential of satellite remote sensing for detecting permanently flooded or intermittently exposed open water surfaces, but many challenges exist, especially for mapping forested wetlands (Ozesmi & Bauer, 2002). Forested wetlands in areas of low topographic relief, such as the Coastal Plain of the Chesapeake Bay Region, are particularly difficult to map, because the forest canopy often obscures the water beneath the canopy during the growing season, and trees found in this type of wetland are often spectrally similar to those found in upland forests (Lang, McCarty, Oesterling, & Yeo, 2013). Lang and McCarty (2009) demonstrated that airborne Light Detection And Ranging (LiDAR) intensity data can be used to detect inundation over forested wetlands during the leaf-off season. Currently, however, routine use of LiDAR data for mapping wetlands and their dynamics over large areas is not feasible due to high data cost and limited data availability.

The main purpose of this study was to develop a new approach for mapping inundation over mostly woody wetland areas using airborne LiDAR data and Landsat images. In this approach, available airborne LiDAR data were used to produce high resolution inundation maps following the method developed by Lang and McCarty (2009). These maps were overlaid on the 30-m grids defined by the Landsat data to calculate subpixel inundation percentage (SIP) within each grid cell. The LiDAR based SIP data were then used to model relationships between inundation and the spectral data acquired by the Landsat. Inundation maps outside the area covered by available LiDAR data and in different dates were then derived by applying the developed model to available Landsat images. We demonstrated the effectiveness of this approach for mapping wetland inundation and change within the upper Choptank River sub-watershed over the Delmarva Peninsula, and evaluated the relationships between the mapped inundation changes and local drought conditions and stream flow. The developed approach will be most effective when the LiDAR and Landsat images are acquired during the leaf-off season. As mentioned earlier, surface water is often obscured by the forest canopy present during the leaf-on growing season.

2. Data and methods

2.1. Study area

The study area included a sub-watershed located within the 1756 km^2 Choptank River watershed on the Delmarva Peninsula within the Coastal Plain Physiographic Province of the Chesapeake Bay Watershed (Fig. 1). This area is referred to as the upper Choptank River sub-watershed throughout this paper. The Choptank River is a major

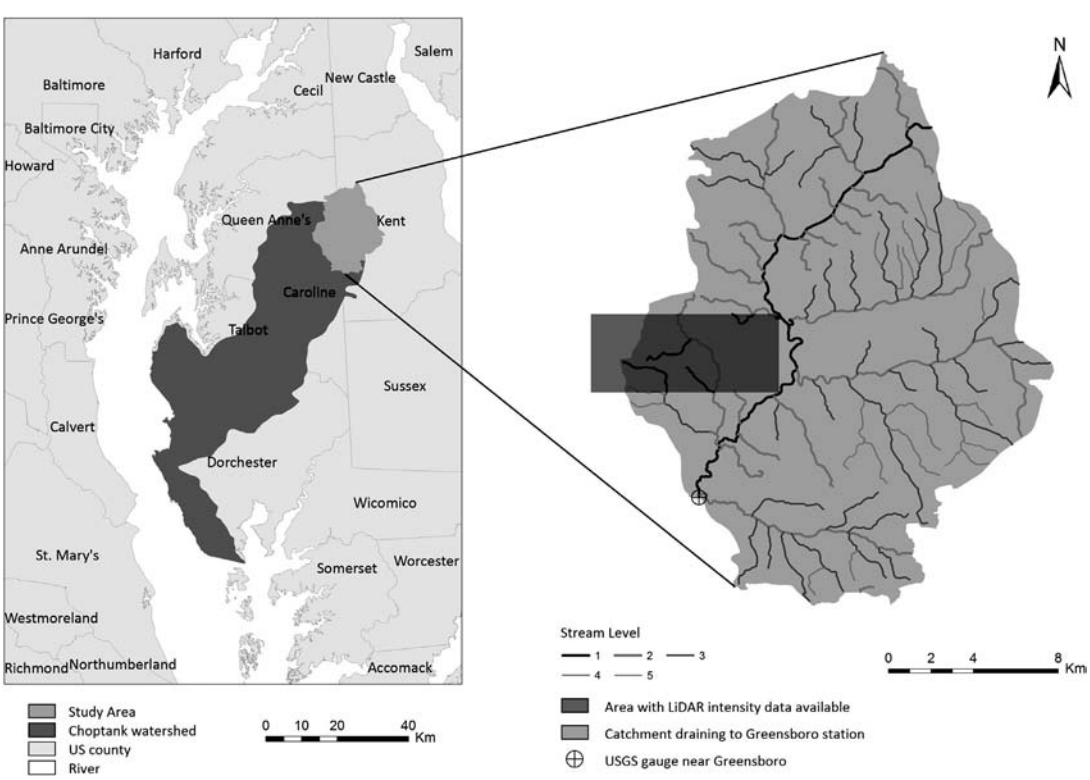

Fig. 1. Location of the upper Choptank River sub-watershed.

tributary of the Chesapeake Bay, originating in Kent County, Delaware and flowing southwest toward its outlet near Cambridge, Maryland. The Choptank River suffers from poor water quality, mainly due to relatively high levels of nutrients, sediment, and bacteria (McCarty et al., 2008). The area is relatively flat (maximum elevation <30 m above sea level) and its land cover is dominated by agriculture (~60%), with smaller amounts of forest (33%) and urban/suburban areas (7%) (McCarty et al., 2008). The area is characterized by a temperate, humid climate with an average annual precipitation of 120 cm/yr (Ator, Denver, Krantz, Newll, & Martucci, 2005). Precipitation is evenly distributed throughout the year and approximately 50% of annual precipitation recharges ground water or enters streams via surface flow, while remaining precipitation is lost to the atmosphere via evapotranspiration (Ator et al., 2005).

The upper Choptank River sub-watershed has a significant amount of forested wetlands. While riparian wetlands and wetland flats are common, the relatively dense distribution of wetland depressions is particularly notable. As mentioned earlier, most wetlands in this area are inundated or saturated for a relatively short period in the spring. The period of maximum hydrologic expression (i.e., highest groundwater level and most area inundated) varies with inter-annual fluctuations in weather conditions, but typically takes place in or around March/April when evapotranspiration has been relatively low. Stream flows are typically high during February through April.

2.2. Data and preprocessing

The inundation mapping approach consisted of two major steps. The first was to model the statistical relationships between subpixel inundation percentage (SIP) and Landsat spectral data using reference samples. The second was to use the derived models to predict SIP in different years and over areas where reference data were not available (Fig. 2). The primary datasets required for this approach included airborne LiDAR intensity data and Landsat images (Table 1).

2.2.1. LiDAR data

Two LiDAR datasets were collected for a 33 km^2 portion of the study area (Fig. 1), one on March 27, 2007 and the other on March 24, 2009. These two years were selected to represent average (2007) and dry (2009) conditions based on the NOAA Palmer Z Index (NOAA National Climate Data Center, http://cdo.ncdc.noaa.gov). As discussed in Section 2.1, end of March is the approximate average period of maximum hydrologic expression when annual inundation levels are typically at their highest. No precipitation occurred during the week before the acquisition of each dataset.

Both LiDAR datasets were collected using an Optech ALTM 3100 sensor with a wavelength of 1064 nm. Their geolocation accuracies were evaluated using over 100 precision GPS points collected in areas of stable elevation (e.g., road intersections) using a Trimble RTK 4700 GPS/base station combination and a surveyed benchmark provided by the Maryland State Highway Administration. The 2007 dataset was collected with a scan angle of +/−20° at a height of 610 m above the Earth's surface with a pulse rate of 100,000 Hz and a scan frequency of 50 Hz. The 2009 dataset was collected at about the same height, but with a scan angle of +/−10°, a pulse rate of 100,000 Hz, and scan frequency of 70 Hz. Bare earth points were classified by the data provider using the Terrascan v7.0 software. The resultant data had vertical errors of ≤0.15 m. The average point densities were 2.5 pts/m^2 (0.40 m post spacing) and 11 pts/m^2 (0.09 m post spacing) in the 2007 and 2009 datasets, respectively. More detailed description of these two datasets has been provided by Lang and McCarty (2009).

2.2.2. Landsat images

The Landsat images were selected to have minimum or no cloud cover over the study area and have acquisition dates as close to those of the LiDAR datasets as possible (Table 1). To evaluate the applicability of the developed approach to other years, two additional Landsat images were selected, one acquired on February 18, 2005 and the other on March 21, 2010, representing average (2005) and wet (2010) years.

The selected images were downloaded from the GLOVIS website of the US Geological Survey (http://glovis.usgs.gov) as level 1T (L1T) products. L1T Landsat images have been calibrated using best available radiometric calibration methods (Chander, Markham, & Helder, 2009) and typically have geolocation accuracy better than 30 m. Therefore, no further geometric correction was performed for the selected images. Radiometrically, the selected images were first converted to top-of-atmosphere (TOA) reflectance, and then atmospherically corrected to produce surface reflectance (SR) using the Landsat Ecosystem Disturbance Adaptive Processing System (LEDAPS) (Masek et al., 2006). The LEDAPS atmospheric correction algorithm adjusts for gaseous absorption, Rayleigh scattering, and Mie (aerosol) scattering using the MODIS/6S radiative transfer model (Vermote et al., 1997). It produces surface reflectance values that are close to in situ reflectance measurements (Gitelson et al., 2012), and are consistent with MODIS reflectance

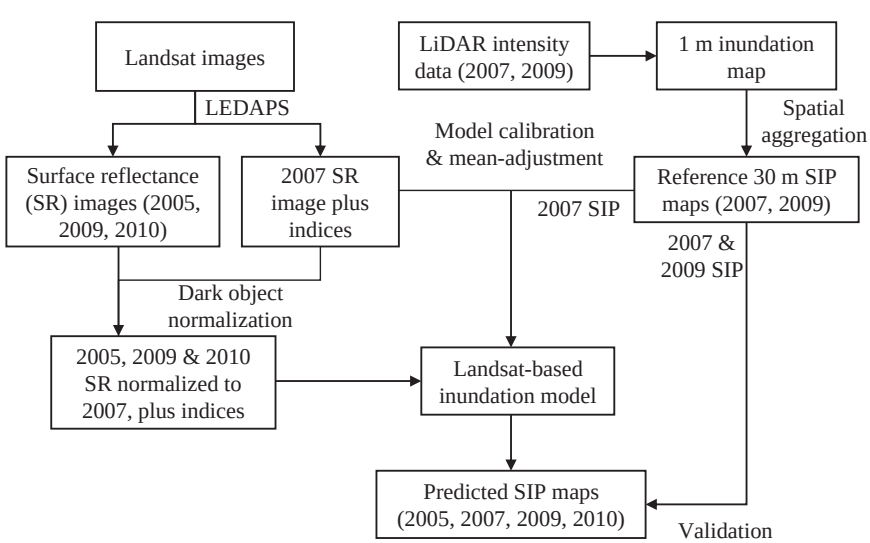

Fig. 2. Flow chart of the approach for developing and validating subpixel inundation percentage (SIP) maps using Landsat and LiDAR intensity data.

Table 1
Acquisition dates or date ranges (yyyy/mm/dd) of the datasets used in this study.

Year	Lidar data	Landsat image	Palmer Z-score index	Water discharge
2005		2005/02/18	2005/01/01–2005/02/28	2005/02/15–2005/02/18
2007	2007/03/27	2007/03/29	2007/02/01–2007/03/31	2007/02/26–2007/03/29
2009	2009/03/24	2009/03/18	2009/02/01–2009/03/31	2009/02/15–2009/03/18
2010		2010/03/21	2010/02/01–2010/03/31	2010/02/18–2010/03/21

products (Feng et al., 2012, 2013) and reflectance values calculated using aerosol data available from Aerosol Robotic Network (AERONET) (Masek et al., 2006).

We noticed some differences between the SR values of water pixels that had SIP values of 100% in the four Landsat images (Table 2). Such differences may arise from incomplete atmospheric correction and/or changes in water turbidity or other factors that affected water reflectance values (Schott, 2007). Although the absolute values of these differences were small, they could be significant when compared with the generally low reflectance values of water. With inundation being the model target, such differences, which were not related to changes in inundation level, could hinder the prediction accuracy when a model derived for one year was applied to a different year. This was confirmed when a preliminary model developed using the 2007 data was applied to the 2009 and 2010 Landsat images—inundation was severely underestimated for those two years. To mitigate this problem, the 2007 image was used as a reference to normalize the 2005, 2009, and 2010 images (target) using a method similar to a dark object subtraction approach (Chavez, 1996). Specifically, the reflectance values of water pixels listed in Table 2 were used to calculate differences between 2007 and the other three years. Those differences were then used to normalize each of the three images such that water pixels that had SIP values of 100% had roughly the same spectral values in all four years. Here the 2007 Landsat image was chosen to be the reference because this image and the 2007 LiDAR based reference inundation dataset were used to establish the inundation models (see more details in Section 2.3.2).

The 2007 image and the normalized images for the other three years were then used to calculate a suite of indices, including tasseled cap brightness (TCB), greenness (TCG), and wetness (TCW), tasseled cap wetness-greenness difference (TCWGD), tasseled cap angle (TCA), the normalized difference vegetation index (NDVI), two forms of the normalized difference wetness index (NDWI), an infrared-visible ratio (IVR) index, and an infrared ratio (IR) index. These indices had been found useful for wetland characterization in previous studies (Table 3). In this study, they were examined in addition to the 6 original Landsat bands for wetland inundation modeling. TCB, TCG, and TCW were calculated following Crist (1985). Equations for calculating the other indices are provided in Table 3.

2.2.3. Reference inundation data

The LiDAR dataset acquired in each of the two dates was first interpolated using an inverse weighted distance (IDW) method to produce a 1-m gridded intensity image. The intensity image was then filtered using an enhanced Lee filter (Lee, 1980) five times with gradually increasing kernel sizes of 3 (twice), 5, 7, and 9 to reduce noise. The filtered intensity image was then used to separate inundated (100% inundated), transition (partly inundated) and non-inundated (0% inundated) pixels. Because the LiDAR instrument used in this study operated at a wavelength (1064 nm) where water has strong absorption, inundated areas typically appeared very dark in the LiDAR intensity images while areas not inundated were in general bright. Transition areas (partly inundated) as well as some green vegetation (mostly evergreen forests) were in between. The threshold values for separating these three classes were derived based on local knowledge (Lang & McCarty, 2009). The inundation

Table 2
Mean reflectance values (%) of collocated water pixels derived using the LEDAPS for the four images used in this study (B1–B7 refers to Landsat band 1 to band 7). These values were used to further normalize the 2005, 2009, and 2010 images such that they had the same mean water reflectance values as the 2007 image.

Year	B1	B2	B3	B4	B5	B7
2005	3.76	4.73	3.69	1.92	0.59	0.38
2007	3.68	5.24	3.45	1.79	0.6	0.45
2009	6.42	6.57	4.7	3.7	1.93	1.36
2010	3.94	4.04	2.55	1.84	0.38	0.25

Table 3
Spectral indices that were used together with the 6 Landsat spectral bands and tasseled cap brightness (TCB), greenness (TCG) and wetness (TCW) in inundation modeling.

Spectral Index	Formula	Reference
NDVI	(Band 4 − Band 3) / (Band 4 + Band 3)	Tucker (1979)
NDWI-1	(Band 4 − Band 5) / (Band 4 + Band 5)	Gao (1996)
NDWI-2	(Band 3 − Band 5) / (Band 3 + Band 5)	Rogers and Kearney (2004)
TCWGD	TCW − TCG	This study
TCA	Arctan (TCG / TCB)	Powell et al. (2010)
IVR	Band 5 / Band 2	Ozesmi and Bauer (2002)
IR	(Band 5 − Band 7) / (Band 5 + Band 7)	Ruan, Feng, and She (2007)

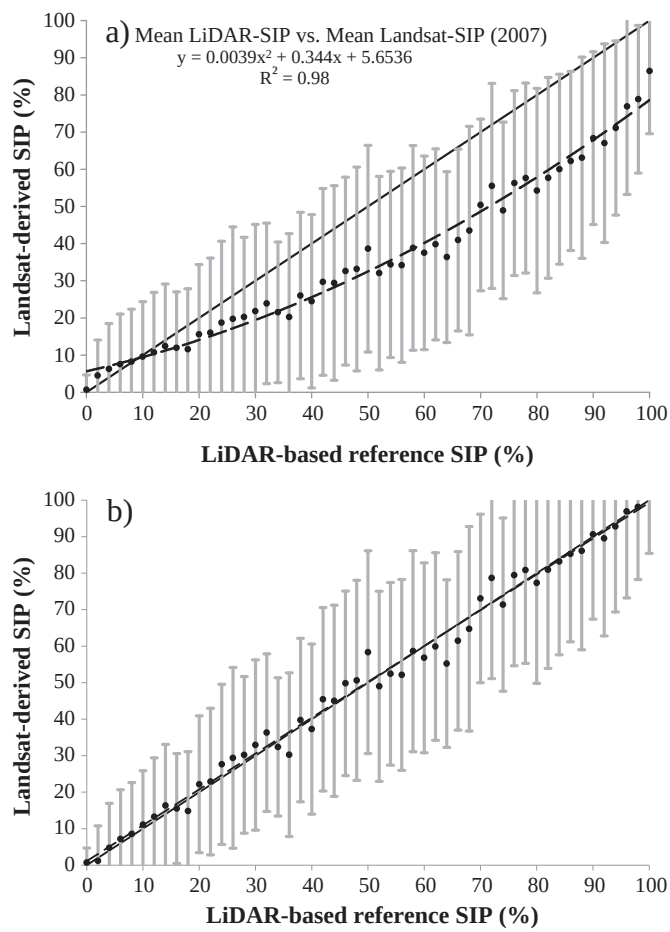

Fig. 3. The mean SIP values of the initial RT prediction for 2007 were mostly lower than the mean reference SIP values within 2% bins of the 2007 reference SIP map (a). Most of these biases were corrected by fitting a 2nd order polynomial function between the mean reference values and the mean predictions (b). In both figures, the mean prediction and its standard deviation within each 2% bin are shown in a black dot and a gray bar, respectively. The solid and dashed lines represent the 1:1 and fitted lines, respectively.

Table 4
Coefficient of determination (R^2) of the linear relationship between sub-pixel inundation percentage (SIP) and Landsat bands and derived indices.

B1	B2	B3	B4	B5	B7	NDVI	NDWI-1
0.16	0.18	0.17	0.25	0.32	0.22	0.00	0.00
NDWI-2	TCB	TCG	TCW	TCWGD	TCA	IVR	IR
0.01	0.29	0.07	0.22	0.41	0.00	0.02	0.00

Table 5
Root mean square error (RMSE) and coefficient of determination (R^2) of the relationships between predicted subpixel inundation percentage (SIP) and reference data.

	Training data (11,000 pixels)		Test data (25,408 pixels)	
	RMSE (%)	R^2	RMSE (%)	R^2
Stepwise linear regression (SLR)	14.07	0.51	14.26	0.52
Regression tree (RT)	10.57	0.72	12.49	0.64

map derived using the 2007 LiDAR dataset was validated using field data collected at ~1000 locations along random transects through multiple forested areas, and was found to have an overall classification accuracy of 96.3% (Lang, McDonough, McCarty, Oesterling, & Wilen, 2012). More details on inundation classification using the 2007 LiDAR dataset have been provided by Lang and McCarty (2009). The same method was used to derive a 1-m inundation map based on the 2009 LiDAR data. No ground data was collected in 2009 for validating this inundation map. We assumed it had a similar level of accuracy as the 1-m inundation map derived using the 2007 Lidar dataset, because both maps were derived based on similar datasets using the same method.

The 1-m inundation map derived for each date was overlaid on the 30-m grids of the Landsat data to calculate subpixel inundation percentage (SIP) at the 30-m resolution. Inundated and non-inundated 1-m pixels were assigned 100% and 0% inundation, respectively. Most of the 1-m transition pixels were partly inundated, and were assigned an average inundation value of 50%, because their exact inundation value could not be determined according to the LiDAR data. Some of the 1-m transition pixels were not inundated, including evergreen forests and dark pavements in urban build-up areas, and therefore were assigned an inundation value of 0%. Based on local expert knowledge (A. Baldwin and D. Whigham, personal communication) and our field experiences in the Delmarva region, evergreen species rarely occur over inundated areas. In this study, evergreen forests were identified based on NWI (http://www.fws.gov/wetlands, accessed in March, 2013) and C-CAP (http://www.csc.noaa.gov/digitalcoast/data/ccapregional, accessed in March, 2013) wetland maps. Once all 1-m

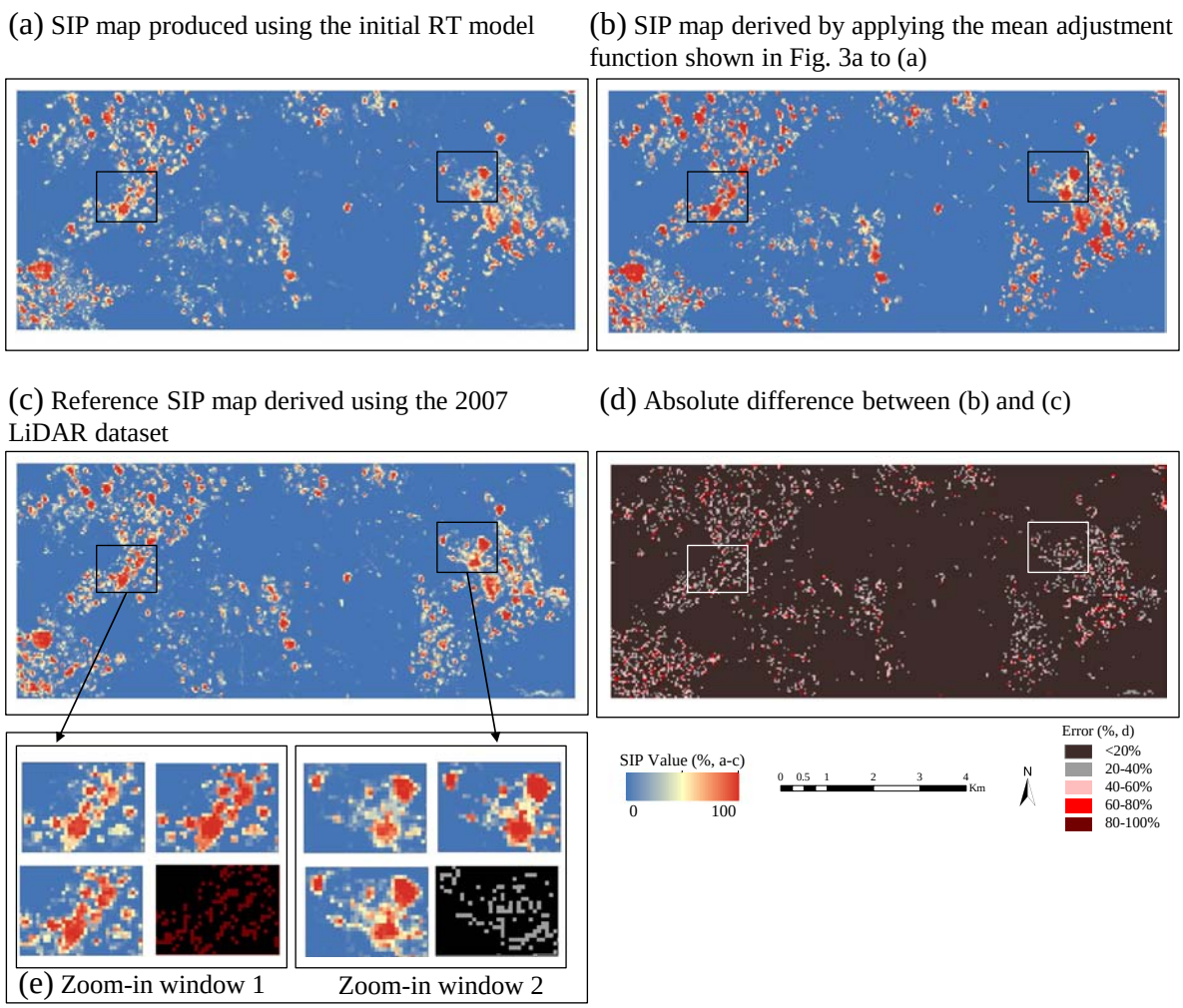

Fig. 4. Comparison of the initial RT predictions for 2007 (a), the mean corrected SIP map (b), and the 2007 reference SIP map (c). Most of the large differences between (b) and (c) were associated with small inundation patches or were located along the edges of larger inundation patches (d), which is better illustrated through two zoon-in windows (e). In each zoom-in window, the four graphics are arranged in the same order as (a) to (d).

pixels were assigned appropriate inundation values, the subpixel inundation percentage (SIP) at the 30-m resolution was calculated as the average of the inundation values of all 1-m pixels within each 30-m grid.

2.3. Inundation modeling

2.3.1. Modeling approaches

We explored three approaches for modeling the relationships between SIP and Landsat data, including correlation analysis, stepwise linear regression (SLR), and regression tree (RT) that represented increasing sophistication in terms of both model inputs and model complexity. The main purpose of the correlation analysis was to understand the relationships between SIP and individual variables derived using Landsat data, including the original spectral bands and derived indices (Table 2), while the SLR and RT were used to derive models with better prediction accuracy. The SLR assumes a linear relationship. Given the many available predictor variables listed in Table 2, SLR was used to identify those that provided the most predictive power and remove those that did not contribute to overall predictive performance (Effroymson, 1960). However, the assumption of a globally linear relationship between SIP and the spectral data may not hold for wetland inundation. Use of nonlinear curve fitting methods in such cases would require a priori knowledge on the mathematical form of a nonlinear relationship. The RT algorithm can approximate complex nonlinear relationships without such a priori knowledge (Breiman, Friedman, Olshend, & Stone, 1984; Huang & Townshend, 2003). A basic regression tree algorithm typically produces a set of rules in a decision tree format, which can be interpreted to show how the independent variable is correlated with the predictor variables under different conditions (De'ath & Fabricius, 2000). Many computer software packages that implement RT also incorporate ensemble and/or bootstrap techniques to improve prediction accuracy (e.g. Breiman, 2001). Ensemble or bootstrapped RT often produces a large number of trees, and the final prediction for each unseen sample is a weighted sum of the predictions of all trees (Chan, Huang, & DeFries, 2001). As a result, the rules in ensemble or bootstrapped trees are not as interpretable as those in a basic regression tree. RT has been implemented in many computer software packages. The Cubist package was used in this study (see http://www.rulequest.com/cubist-info.html for more details on this package). This package has been used to model land cover and biophysical variables using remote sensing data in many studies (e.g. Blackard et al., 2008; Walker, Kellndorfer, LaPoint, Hoppus, & Westfall, 2007).

2.3.2. Model calibration and testing

Both reference SIP datasets derived using 2007 and 2009 LiDAR data could be used to develop the statistical models described in Section 2.3.1. In this study the 2007 dataset was selected for model development, because (1) 2007 was a year with average conditions; (2) the 2007 inundation map had been validated using field observations and was found highly accurate (Lang et al., 2012); and (3) the acquisition dates of the 2007 LiDAR dataset and Landsat image were closer than those of the 2009 datasets. For the correlation analysis, all 30-m SIP pixels derived from the 2007 LiDAR data were used. For SLR and RT, a random sample of 30% of those pixels (11,000 pixels in total) was used as training data. The remaining 70% (25,408 pixels in total) were used as test data to evaluate the SLR and RT models derived from the training data.

Training and test accuracies of the SLR and RT models were measured using root mean square error (RMSE) and the coefficient of determination (R^2) of the relationships between the LiDAR-based and Landsat-predicted SIP values:

$$RMSE = \sqrt{\sum_{i=1}^{N}\left(SIP_p - SIP_r\right)^2 / N}$$

where SIP_p and SIP_r are the predicted and reference SIP values, respectively, and N is the total number of samples.

The 2009 reference SIP dataset was used to demonstrate the applicability of the final SIP model derived using the 2007 reference dataset to other years. Specifically, it was used to evaluate the predictions derived by applying the 2007 SIP model to the 2009 Landsat image. Predictions of the 2007 SIP model for 2005 and 2010 were evaluated qualitatively using the Landsat images of those two years. No other reference SIP data were available for an independent assessment for these two years.

2.3.3. Model prediction, mean adjustment, and inundation change analysis

As will be discussed in Section 3, the RT model was more accurate than the SLR model and therefore was selected to produce SIP maps for the study area. However, this model also underestimated SIP substantially for areas with SIP values > 20%. The mean of the predicted SIP values were substantially lower than those of the 2007 reference data at all inundation levels above 20% (see Fig. 3a in Section 3.1.3). To correct for such biases, we divided the LiDAR-based SIP values in the 2007 training dataset into 2% bins. Mean LiDAR-based and Landsat-predicted SIP values were then calculated separately for each bin. These two sets of mean SIP values were then used to derive a polynomial function, which was then applied to the RT predictions to remove the biases in the mean SIP values. The 2% binning range was chosen based on a heuristic analysis of the RT predictions. This binning range

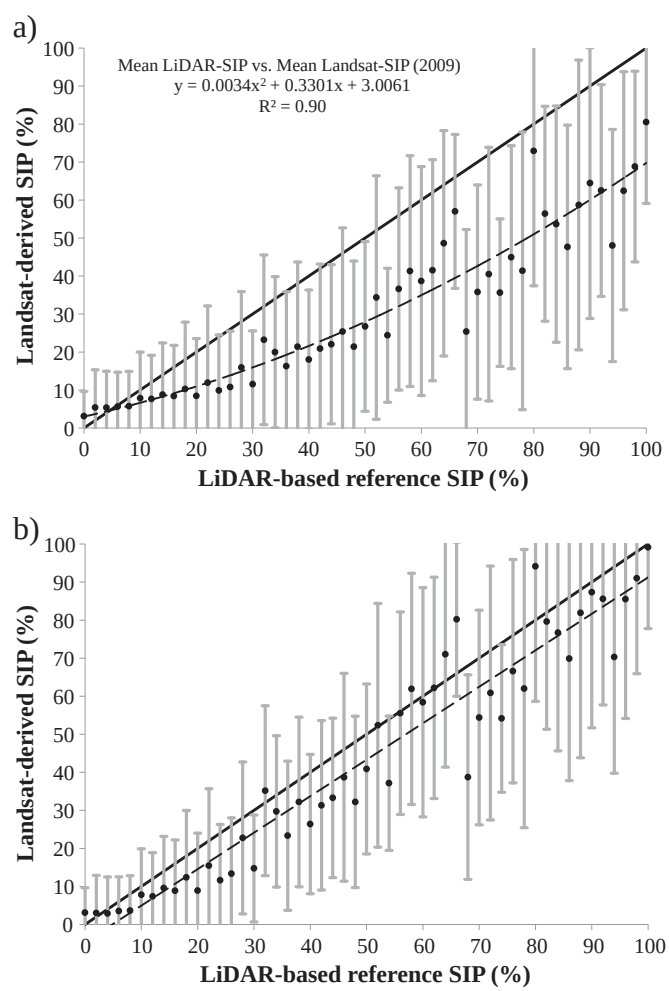

Fig. 5. The mean SIP values of the initial RT prediction for 2009 were also mostly lower than the mean reference SIP values within 2% bins of the 2009 reference SIP map (a). Most of these biases were corrected by the 2007 polynomial function shown in Fig. 3a, which resulted in residual biases of about 5% (b). See Fig. 3 for explanations of the black dot, gray bar, solid line and dashed line.

produced a relatively large number of data points (50) for fitting polynomial functions up to the 3rd order while allowing each bin to have enough data values for calculating a mean and its standard deviation. The standard deviation revealed that most of the bins appeared to have similar levels of variance (Fig. 3a).

The final RT model and the mean adjustment polynomial function were applied to the 2007 Landsat SR image as well as the radiometrically normalized images for the other three years to produce SIP maps for all four years. These maps were then used to calculate inundation changes over the entire study area.

We evaluated whether the derived inundation changes were correlated with changes in local drought condition and stream flow. Local drought condition was measured using a 2-month average Palmer Z-score index obtained from the National Climate Data Center of the National Oceanic and Atmospheric Administration (NOAA NCDC, http://www.ncdc.noaa.gov/oa/climate/research/prelim/drought/palmer.html. Last accessed in March, 2013). For each of the four years considered in this study, the 2-month period included the acquisition month of the Landsat image and the previous month (Table 2). Stream flow was a 4-day (including the acquisition day of each Landsat image and the previous three days, Table 2) average of water discharge measured at the USGS streamgage station near Greensboro, Maryland (See location shown in Fig. 1) (http://waterdata.usgs.gov/nwis/rt/. Last accessed in March 2013).

3. Results

3.1. Inundation modeling using Landsat data

3.1.1. Correlations between SIP and Landsat spectral data

Relationships between SIP and individual Landsat bands and spectral indices were quantified using the coefficient of determination (R^2) (Table 4). Among the sixteen variables tested (Table 3), the difference between TCW and TCG (TCWGD) had the highest R^2 value. The 41% SIP variance explained by this variable was substantially higher than the 22% explained by TCW alone. In general, TCW is considered a good indicator of water and soil wetness. But it is also sensitive to the moisture content of green vegetation (Crist & Cicone, 1984; Stoner & Baumgardner, 1981). The Landsat images used in this study had some green vegetation, mostly evergreen forests, although they were acquired during the leaf-off season. Derived by subtracting TCG from TCW, TCWGD should be less sensitive to green vegetation than TCW. Several other variables, including bands 5, 4, 7, and TCB, which were highly correlated among themselves, also had R^2 value of >20%. But some of the other indices that were found useful for wetland characterization in previous studies, including NDVI, NDWI-1, NDWI-2, TCA, IVR, and IR, had little or no correlation with SIP ($R^2 < 0.1$) in this study. It should be noted that this does not mean these variables are not useful for inundation modeling. In fact, many of them were used heavily by the SLR and RT models discussed in Section 3.1.2.

3.1.2. Performance of the SLR and RT models

By using multiple variables, both SLR and RT yielded better relationships between predicted and LiDAR-based SIP values than the best relationships that could be derived using a single variable (Table 5). The SLR model had an R^2 value of 0.51 when evaluated using the training data. Predictor variables selected by this model included the 6 original Landsat spectral bands plus all indices derived through nonlinear transformation of those bands, including NDVI, NDWI-1, NDWI-2, TCA, IVR, and IR. The four tasseled cap indices (TCB, TCG, TCW, and TCWGD) were not selected because they were simply linear combinations of the 6 spectral bands, although individually three of them had relatively high correlations with SIP (Table 4). The R^2 value was further improved to 0.72 when RT was used instead of SLR, and model error as measured using RMSE was reduced from 14.07% to 10.57%. Overfitting was not a major issue for both the SLR and RT models. They had slightly higher

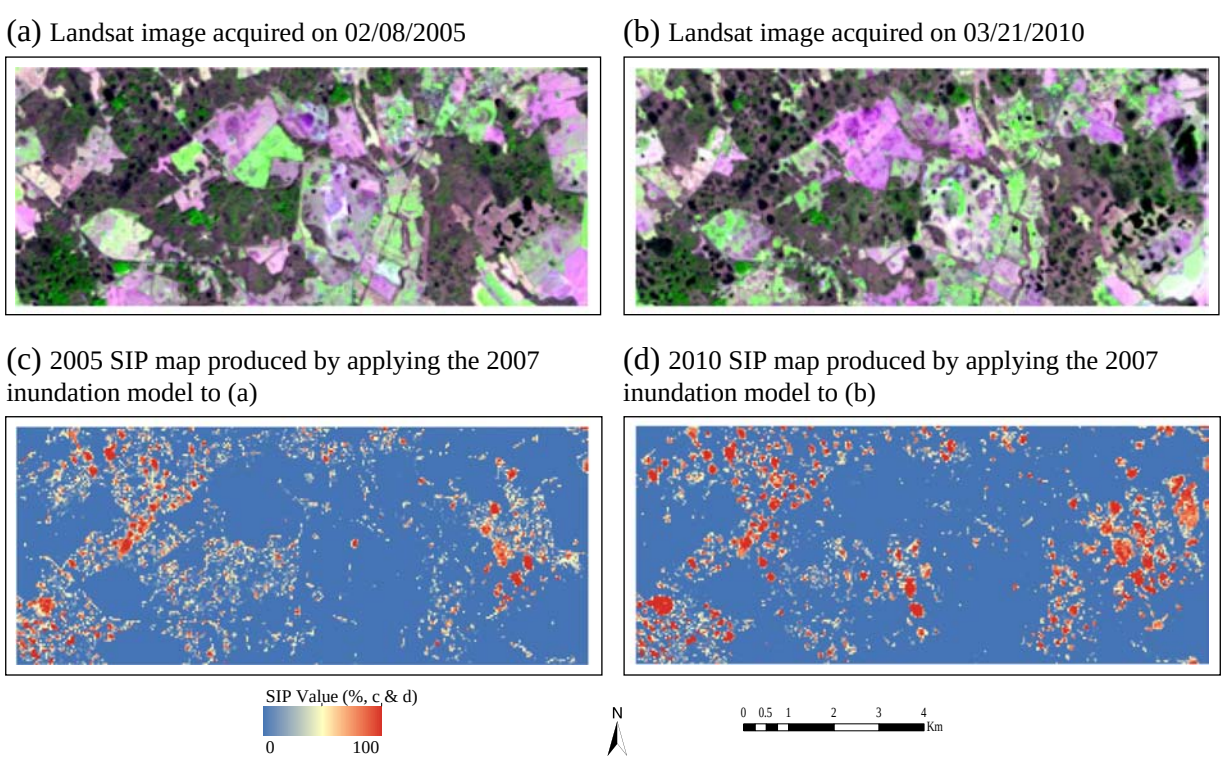

Fig. 6. 2005 (c) and 2010 (d) SIP maps predicted by applying the inundation model derived using 2007 data to the Landsat images acquired in 2005 (a) and 2010 (b), respectively. The two Landsat images are shown with bands 5, 4, and 3 in red, green, and blue. Open water bodies and pixels with high SIP values should look dark in these images. Visually the inundation patterns in the two SIP maps matched those seen in the input Landsat images.

RMSE values when evaluated using the test dataset than using the training dataset, although for the RT model the test dataset yielded a lower R^2 value than the training dataset.

Given the complex, likely nonlinear relationships between SIP and the spectral values of Landsat data, the better performance of RT as compared with SLR was expected, because RT can approximate complex nonlinear relationships by partitioning a dataset into subsets such that the relationship within each subset can be simplified to a linear model (Huang & Townshend, 2003). This is consistent with observations made in many previous studies (e.g. Li et al., 2011; Yang, Huang, Homer, Wylie, & Coan, 2003). Therefore, the RT model was used to predict inundation for the entire study area.

3.1.3. Effectiveness of mean adjustment

An examination of the RT predictions revealed that the predicted mean values for SIP > 20% were substantially lower than the mean reference SIP values (Fig. 3a). These biases likely were related to the extremely unbalanced training data distribution—over 60% of the training samples had a SIP value of 0% and more than half of the remaining had SIP values of <20%. By dividing the reference SIP values into 2% bins, the relationship between the mean predictions and mean reference SIP values within those bins could be approximated using a second order polynomial function ($R^2 = 0.98$, Fig. 3a). By adjusting the initial RT prediction using this polynomial function, most of the biases between the mean values of the original RT prediction and the mean reference SIP values were removed (Fig. 3b), although this resulted in an increase in the RMSE from 12.49% to 15.16%.

A comparison between the SIP map produced by the initial RT model (Fig. 4a) and the reference SIP map (Fig. 4c) shows that many wetland patches with very high SIP values were under-predicted by the initial RT model. After applying the mean adjustment function, the under-predictions were greatly reduced, and the wetland patches with high SIP values appeared to better match those in the reference SIP map (Fig. 4b). Further examination of the errors in the final SIP map derived after mean adjustment (Fig. 4d) revealed that those errors were small in non-inundated areas (SIP = 0%) or areas with SIP > 50%. Over 90% of

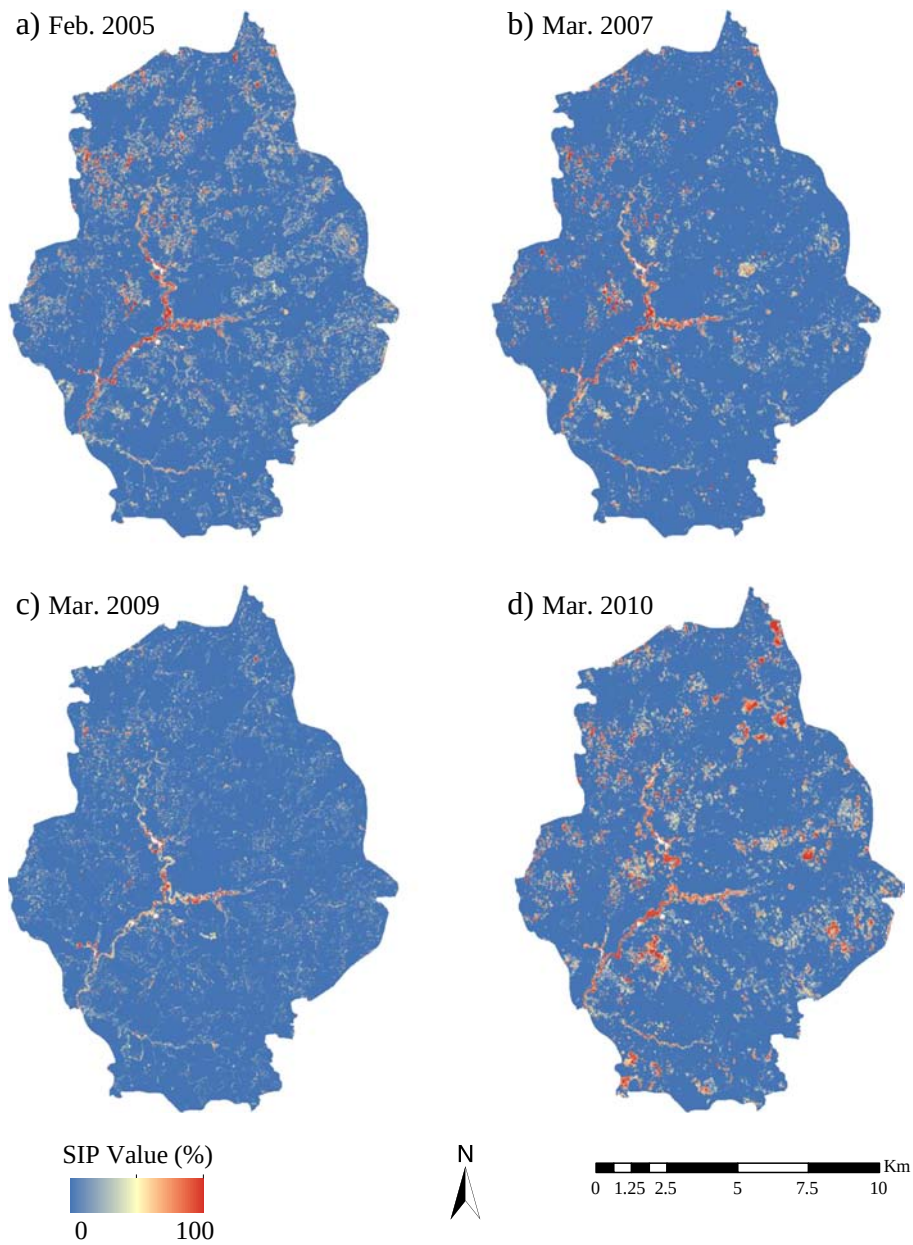

Fig. 7. Final SIP maps for the upper Choptank River sub-watershed derived using the inundation modeling approach developed in this study.

the area covered by the LiDAR data and 85% of the forested areas had prediction errors of less than 20%. Most of the larger errors appeared to be associated with residual misregistration errors between the LiDAR data and the Landsat images (up to 1–2 30-m Landsat pixels), as they were often located around small inundation patches or along the edge of larger patches (Fig. 4(d & e)).

3.1.4. Applicability of the 2007 models to other years

To evaluate whether the RT model and the mean adjustment function developed for 2007 could be applied to other years, we directly applied them to the 2005, 2009, and 2010 Landsat images that were radiometrically normalized as described in Section 2.2.2. The resulting SIP maps for 2009 were evaluated using the reference SIP map derived using the 2009 LiDAR dataset. Fig. 5a shows that the mean predictions of the initial RT model for 2009 had biases similar to those seen in the 2007 RT predictions (Fig. 3a). A mean correction polynomial function could be derived using the 2009 reference SIP dataset (Fig. 5a), but that function was not statistically different from the one derived using 2007 data (p-value = 0.09), suggesting that the 2007 mean adjustment function in Fig. 3a could be applied to 2009 and the other two years. Fig. 5b shows that most of the biases in the 2009 predictions were removed using the 2007 mean adjustment polynomial function shown in Fig. 3a, although there seemed to have residual biases of ~5% in SIP value.

No LiDAR based reference SIP data were available for either 2005 or 2010; hence quantitative validation of the final SIP maps for those two years was not possible. However, visual examination of the 2005 Landsat image (Fig. 6a) revealed that the inundation patterns as seen in that image matched the final SIP map derived by applying the 2007 models to the 2005 image (Fig. 6c). Similarly, the inundation patterns seen in the 2010 Landsat image (Fig. 6d) matched those predicted by applying the 2007 models to the 2010 image (Fig. 6b). Therefore, the inundation models derived using the 2007 data were deemed robust enough for producing SIP maps for the other three years after the Landsat images acquired for those years were radiometrically normalized to the 2007 image as described in Section 2.2.2.

3.2. Inundation changes within the upper Choptank River sub-watershed

Fig. 7 shows the SIP maps over the upper Choptank River sub-watershed derived by applying the final RT model and mean adjustment function to the Landsat images acquired in 2005, 2007, 2009, and 2010. Inundation was highest in 2010, followed by 2005 and 2007. 2009 had the least inundated areas. To quantify area changes at different inundation levels, we divided the SIP values into 5 classes: non-inundated (SIP < 0.1%), low inundated (0.1% ≤ SIP < 25%), medium inundated (25% ≤ SIP < 50%), high inundated, (50% ≤ SIP < 75%), and near complete inundated (SIP ≥ 75%). Since inundation was the main focus of this study, only the four inundated classes are further discussed in the remaining sections.

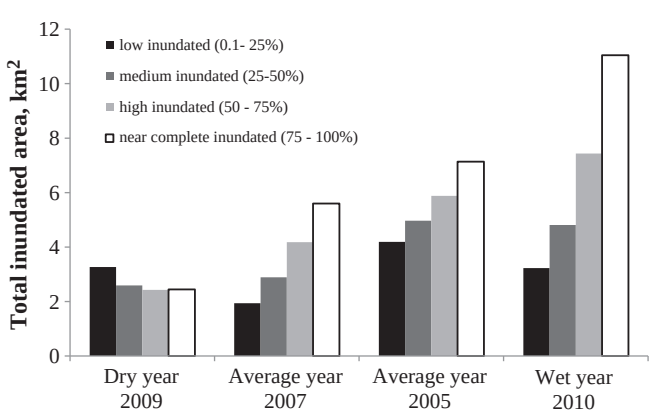

Fig. 8. Changes in the total area of different inundation classes over the upper Choptank River sub-watershed for the four years analyzed.

Fig. 8 shows the total areas of the four inundated classes over the four years, sorted in the order of increasing amount of high and near complete inundation. This order (i.e., 2009, 2007, 2005 and 2010) also corresponds to the wetting trend suggested by the Palmer Z-score index. The total area of the near complete inundated class increased by almost five times in the wet year of 2010 as compared to the dry year of 2009, while that of the high inundated class more than tripled. The medium inundated class also saw some increases from dry to wet years, but the low inundated class did not have a particular trend. Its total area was smaller in the wetter years of 2007 and 2010 than in the drier years of 2005 or 2009.

The inundation changes derived above were correlated with local drought conditions and stream flow (Fig. 9). Both the Palmer Z-score index and water discharge measured at the Greensboro streamgage were highly correlated with the total areas of the high inundated and near complete inundated classes, and to a lesser degree, with the medium inundated class. They were not correlated with the low inundated class, which was expected since area changes in this class did not seem to have any relationship with the dryness or wetness of any particular year.

4. Discussion

Remote sensing provides an economical data source for mapping inundation, one of the most important abiotic attributes of wetlands, across the landscape. Lang and McCarty (2009) have demonstrated that LiDAR intensity data can be used to derive highly reliable inundation

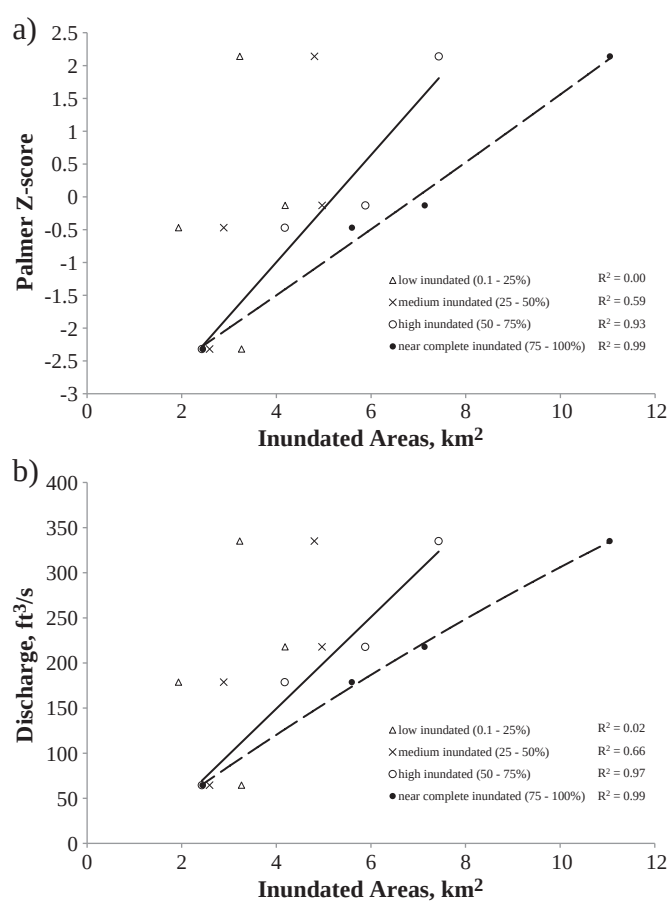

Fig. 9. Relationships between the total area of different inundation classes and a 2-month average Palmer Z-score index (a) and water discharge measured at the gage near Greensboro, MD (b) (see Fig. 1 for location of the gage). Solid and dashed lines are for linear fits to the near complete and high inundated classes, respectively.

classifications. In this study we develop an approach that further integrates LiDAR intensity data and Landsat images to allow for inundation mapping beyond the areas and years covered by available LiDAR data. This approach includes several key elements designed to improve inundation mapping using Landsat data.

First, the use of regression tree instead of uni-variate or multiple linear regression techniques substantially improved the accuracy of inundation modeling, which was consistent with previous observations on the comparative performances of RT and linear regression methods (e.g. Li et al., 2011; Yang et al., 2003). RT predictions were often overestimated in the low end and underestimated in the high end (e.g. Powell et al., 2010; Walker et al., 2007). In this study, underestimation appeared to be the main problem for areas with SIP > 20% (Fig. 3a). But it was correctable using the mean adjustment method developed in this study. As discussed earlier, the underestimation in the initial RT predictions might be related to the fact that the majority of the study area had very low SIP values. We experimented with models developed using training datasets consisting of approximate the same number of samples at different SIP levels, but those models also had underestimations. It should be noted that prediction biases were not unique to RT. We examined the predictions by the SLR model and observed that the mean of the predicted SIP values at different inundation levels had substantial biases too. These observations suggest that use of statistical methods such as SLR or RT to model subpixel land cover components may result in substantial biases when the distributions of the subpixel percentage of those land cover components are highly unbalanced. Such highly unbalanced distributions are common for land cover components like wetland inundation and urban imperviousness, which typically account for very small portions of the total area of a large region. The mean adjustment method developed in this study appeared to be effective in reducing those prediction biases.

Second, although the Landsat images used in this study had been converted to surface reflectance values that were highly consistent with near simultaneous MODIS measurements (Feng et al., 2012, 2013), additional radiometric normalization was necessary. Water pixels with a SIP value of 100% had different mean reflectance values among the four years (Table 2). Although the absolute values of these differences were relatively small (approximately 1%–2%), they accounted for large portions of the spectral signals of water, and therefore could result in large differences in predicted SIP values. Improvement in atmospheric correction algorithms likely won't be able to reduce these differences much further, because those differences were close to or within the calibration uncertainties of the Landsat sensors (Markham & Helder, 2012). Some of the differences were not even related to atmospheric effect, but could have resulted from changes in water conditions (e.g., turbidity, surface vegetation). With the majority of atmospheric effects having been adjusted by the LEDAPS atmospheric correction algorithm, however, the simple dark object subtraction method employed in this study seemed to be effective in removing much of the temporal variations of the reflectance values of water pixels.

While in the inundation change analysis we divided the SIP values into 5 classes, being able to map inundation as a continuous variable allows analysis using any customized SIP threshold values. As a demonstration, we classified the derived SIP data into binary maps of inundated and non-inundated using SIP threshold values of 0.5%, 1%, 5%, and values between 10% and 90% with a 10% interval, and reexamined the relationships between inundation and river discharge as well as the Palmer Z-score index. When inundation area was calculated as the total area of inundated pixels as classified using the above threshold values, its relationships with river discharge and the Palmer Z-score index (R^2) improved greatly when the SIP threshold value increased from 0.1% to 30%, and continued to improve until the SIP threshold value reached 60% to 80% (Fig. 10a). When inundation area was calculated as the total SIP value of the inundated pixels, however, those relationships were less affected by the SIP threshold value used, especially

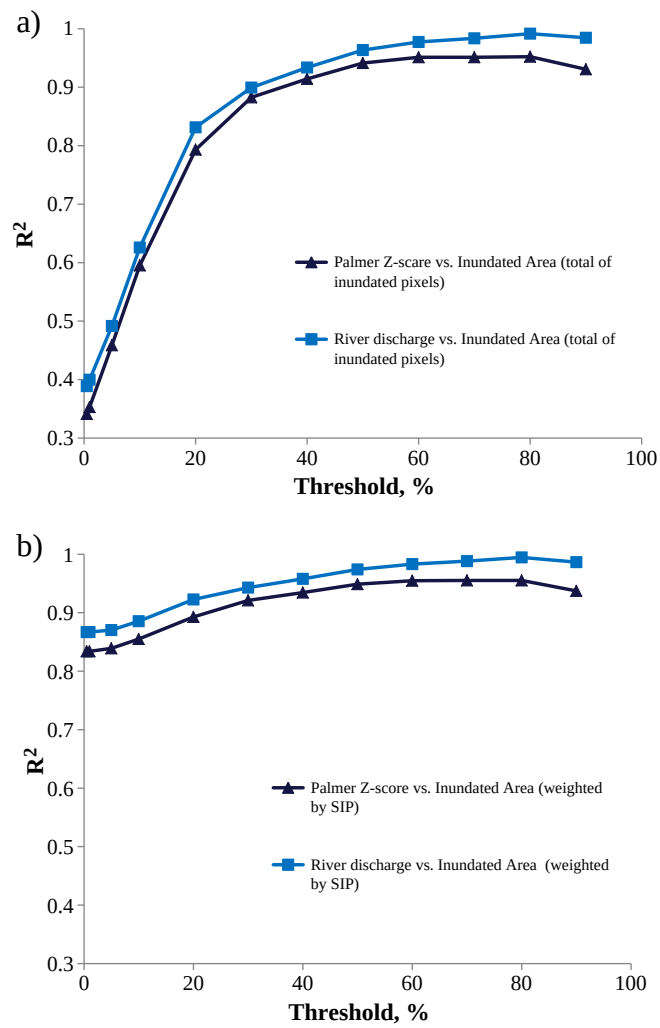

Fig. 10. Relationships (R2) between inundation and water discharge and Palmer Z-score index were sensitive to the threshold value used to separate inundated pixels from non-inundated pixels when inundation was calculated as the total area of inundated pixels (a), but were less so when calculated as the total SIP value of the inundated pixels (b).

when it was below 30% (Fig. 10b). These results suggest that caution should be taken when inundation classifications are used to analyze relationships between inundation and river discharge or local drought index, because the results may be sensitive to the threshold value used to separate inundation from non-inundation. This problem will be greatly reduced by using SIP maps as derived in this study.

The errors in the 30-m SIP maps may be further reduced when the maps are aggregated properly for use in model studies. Currently most hydrology models use grid cells larger than 30-m (e.g. Nelson & Palmer, 2007; Niehoff, Fritsch, & Bronstert, 2002). Huang (1999) demonstrated that for spatial density variables like percent tree cover or SIP, the errors in fine resolution map products can be reduced when those products are aggregated to coarser resolutions through spatial averaging. Depending on the level of spatial autocorrelation among the errors of adjacent pixels at the original resolution, those errors could be reduced by as much as 50% when pixel size is doubled in each dimension. In this study, RMSE values of the 2007 and 2009 inundation maps were reduced from 15.16% to 6.5% and 15.0% to 7.3% respectively, when those maps were aggregated from 30-m to 90-m through spatial averaging (Fig. 11).

Given the global availability of Landsat data, both historically (Goward et al., 2006) and for the foreseeable future (Loveland & Dwyer, 2012), and the fact that LiDAR data are becoming increasingly

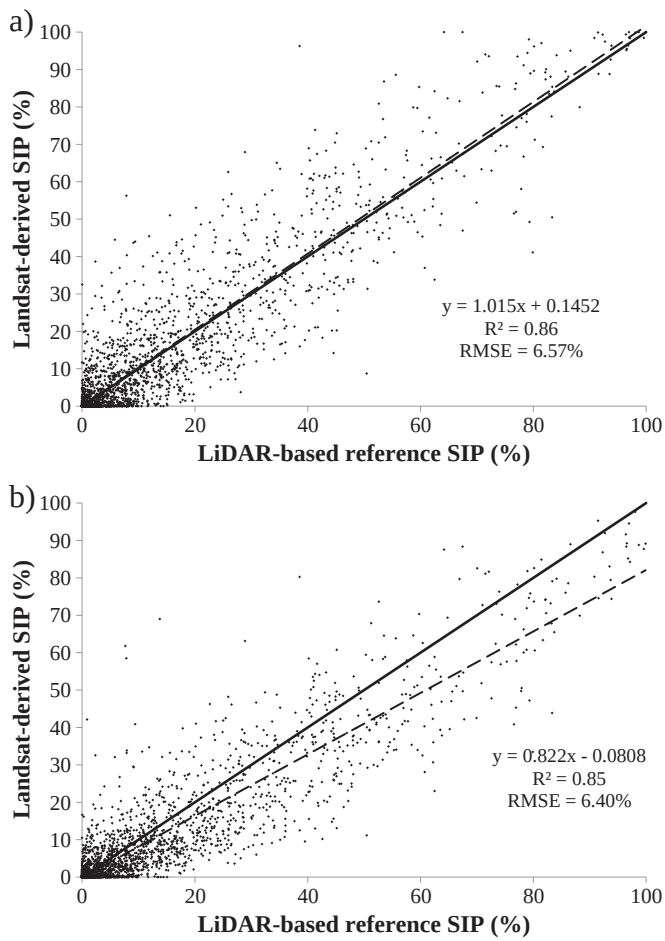

Fig. 11. Relationships between Landsat-derived and reference SIP maps after they were aggregated from 30-m to 90-m for 2007 (a) and 2009 (b). The dashed line shows the best-fit-function of Landsat-predicted and reference SIP values. The solid line is the 1:1 line.

more affordable and are already available in many areas in the United States and other countries, the approach developed in this study has potential for assessing historical inundation changes and for monitoring future changes in many regions. Such large area monitoring cannot be achieved using high resolution datasets, because 1) contiguous coverage of historical high resolution data does not exist in many areas, and 2) the costs for purchasing such data, if exist, would be overwhelming. As with the validation of other types of historical changes (Cohen, Fiorella, Bray, Helmer, & Anderson, 1998; Huang et al., 2010), historical inundation change products are difficult to validate due to lack of reference data. While reference SIP data can be derived using the approach of Lang and McCarty (2009) for areas covered by available LiDAR intensity data, LiDAR data did not become available until the recent decade or so. Alternative data sources need to be explored in validating inundation changes that occurred before LiDAR data became available or over areas not covered by available LiDAR data. In this study, only a qualitative assessment of the 2005 and 2010 SIP maps could be achieved through a visual examination of those maps against the inundation patterns in the input Landsat images. However, the clearly increasing trends of inundated areas (especially the high inundated and near complete inundated classes) from dry to wet years (Fig. 8) and the high correlations between observed inundation changes and local drought index and stream flow (Fig. 9) can attest to the reliability of the inundation maps developed in this study. Such correlations, if present over larger areas and for longer time periods, may be useful for improving model studies of drought, wetland hydrology, and stream runoff.

The inundation mapping approach developed in this study is most effective for use with data acquired during the leaf-off season. It should not be used with data acquired during the leaf-on season, because in forested wetlands, most of the signal from surface water is blocked by the presence of a green canopy cover during that season. Synthetic Aperture Radar (SAR) radar, especially multi-frequency multi-polarization radar, should allow better characterization of flooded forests (Hess, Melack, Filoso, & Yong, 1995; Hess, Melack, & Simonett, 1990), although radar data acquired during the leaf-off season also seemed to yield better results than those acquired during the leaf-on season (Lang & Kasischke, 2008; Lang et al., 2008).

5. Conclusions

Reliable and up-to-date inundation information is essential for improved conservation and management of wetlands to ensure that they provide sustained ecosystem services. In this study, we developed a new approach for mapping wetland inundation using Landsat and LiDAR data, and demonstrated its effectiveness for monitoring wetland inundation change over the upper Choptank River sub-watershed. The results revealed large changes in wetland inundation between dry, average, and wet years, which were highly correlated with local drought conditions and stream flow. The developed approach has potential for deriving historical inundation changes in areas covered by available Landsat and LiDAR data. As the costs of LiDAR data continue to decline while demand increases, such data will become increasingly more available. With the successful launch of the Landsat 8 (also known as the Landsat Data Continuity Mission (LDCM)), global Landsat data will be acquired continuously. Therefore, the approach developed in this study may allow continuous monitoring of ongoing and future inundation changes for increasingly more areas. The strong correlations between wetland inundation and drought conditions and stream flow as demonstrated in this study suggest that the inundation change products derived using this approach may be useful for improving model studies of drought, wetland hydrology, and stream runoff. Further investigations are needed to evaluate whether such relationships exist over larger areas and for longer time periods.

Acknowledgments

This research was funded by the NASA's Land Cover and Land Use Change Program (contract No: NNX12AG21G). Additional support was provided by the NASA's Terrestrial Ecology, Carbon Cycle Sciences, MEASURES programs, NSF-UMD advance program, the Wetland Component of the USDA National Conservation Effects Assessment Project, US Geological Survey, and USDA Forest Service. Comments provided by two anonymous reviewers are highly appreciated.

References

Ator, S. W., Denver, J. M., Krantz, D. E., Newll, W. L., & Martucci, S. K. (2005). *A surficial hydrogeologic framework for the Mid-Atlantic coastal plain*. Reston, VA, USA: USGS Professional Paper, 1–44.

Baker, C., Lawrence, R. L., Montagne, C., & Patten, D. (2007). Change detection of wetland ecosystems using Landsat imagery and change vector analysis. *Wetlands*, *27*, 610–619.

Berberoglu, S., Yilmaz, K. T., & Ozkan, C. (2004). Mapping and monitoring of coastal wetlands of Cukurova Delta in the Eastern Mediterranean region. *Biodiversity and Conservation*, *13*, 615–633.

Blackard, J. A., Finco, M. V., Helmer, E. H., Holden, G. R., Hoppus, M. L., Jacobs, D.M., et al. (2008). Mapping US forest biomass using nationwide forest inventory data and moderate resolution information. *Remote Sensing of Environment*, *112*, 1658–1677.

Breiman, L. (2001). Random forests. *Machine Learning*, *45*, 5–32.

Breiman, L., Friedman, J. H., Olshend, R. A., & Stone, C. J. (1984). *Classification and regression trees*. Belmont, California: Wadsworth International Group, 358.

Castaneda, C., & Ducrot, D. (2009). Land cover mapping of wetland areas in an agricultural landscape using SAR and Landsat imagery. *Journal of Environmental Management*, *90*, 2270–2277.

Chan, J. C. -W., Huang, C., & DeFries, R. S. (2001). Enhanced algorithm performance for land cover classification using bagging and boosting. *IEEE Transactions on Geoscience and Remote Sensing*, *39*, 693–695.

Chander, G., Markham, B.L., & Helder, D. L. (2009). Summary of current radiometric calibration coefficients for Landsat MSS, TM, ETM+, and EO-1 ALI sensors. *Remote Sensing of Environment*, *113*, 893–903.

Chavez, P.S. (1996). Image-based atmospheric corrections—Revisited and improved. *Photogrammetric Engineering & Remote Sensing*, *62*, 1025–1036.

Cohen, W. B., Fiorella, M., Bray, J., Helmer, E., & Anderson, K. (1998). An efficient and accurate method for mapping forest clearcuts in the Pacific Northwest using Landsat imagery. *Photogrammetric Engineering & Remote Sensing*, *64*, 293–300.

Crist, E. P. (1985). A TM tasseled cap equivalent transformation for reflectance factor data. *Remote Sensing of Environment*, *17*, 301–306.

Crist, E. P., & Cicone, R. C. (1984). A physically-based transformation of Thematic Mapper data—The TM Tasseled Cap. *IEEE Transactions on Geoscience and Remote Sensing*, *GE-22*, 256–263.

De'ath, G., & Fabricius, K. E. (2000). Classification and regression trees: A powerful yet simple technique for ecological data analysis. *Ecology*, *81*, 3178–3192.

Effroymson, M.A. (1960). Multiple regression analysis. In A. Ralston, & H. S. Wilf (Eds.), *Mathematical methods for digital computers* (pp. 191–203). New York: Wiley.

Feng, M., Huang, C., Channan, S., Vermote, E. F., Masek, J. G., & Townshend, J. R. (2012). Quality assessment of Landsat surface reflectance products using MODIS data. *Computers & Geosciences*, *38*, 9–22.

Feng, M., Sexton, J. O., Huang, C., Masek, J. G., Vermote, E. F., Gao, F., et al. (2013). A Global Land Survey surface reflectance product: assessment using coincident MODIS observations. *Remote Sensing of Environment*, *134*, 276–293.

Fisher, A. (2000). Preliminary findings from the Mid-Atlantic Regional Assessment. *Climate Research*, *14*, 261–269.

Gao, B. -c. (1996). NDWI—A normalized difference water index for remote sensing of vegetation liquid water from space. *Remote Sensing of Environment*, *58*, 257–266.

Gitelson, A., Peng, Y., Masek, J., Rundquist, D., Verma, S., Suyker, A., et al. (2012). Remote estimation of crop gross primary production with Landsat data. *Remote Sensing of Environment*, *121*, 404–414.

Goward, S., Irons, J., Franks, S., Arvidson, T., Williams, D., & Faundeen, J. (2006). Historical record of landsat global coverage: Mission operations, NSLRSDA, and international cooperator stations. *Photogrammetric Engineering and Remote Sensing*, *72*, 1155–1169.

Green, K. (2006). Landsat in Context: The Land Remote Sensing Business Model. *Photogrammetric Engineering and Remote Sensing*, *72*, 1147–1155.

Groot, R., Stuip, M., Finlayson, M., & Davidson, N. C. (2009). *Valuing wetlands: Guidance for valuing the benefits derived from wetland ecosystem services*. Gland: Ramsar Convention, 45.

Hess, L. L., Melack, J. M., Filoso, S., & Yong, W. (1995). Delineation of inundated area and vegetation along the Amazon floodplain with the SIR-C synthetic aperture radar. *IEEE Transactions on Geoscience and Remote Sensing*, *33*, 896–904.

Hess, L. L., Melack, J. M., & Simonett, D. S. (1990). Radar detection of flooding beneath the forest canopy: A review. *International Journal of Remote Sensing*, *11*, 1313–1325.

Huang, C. (1999). *Improved land cover characterization from satellite remote sensing*. (Dissertation Thesis). College Park: University of Maryland, 218.

Huang, C., Goward, S. N., Masek, J. G., Thomas, N., Zhu, Z., & Vogelmann, J. E. (2010). An automated approach for reconstructing recent forest disturbance history using dense Landsat time series stacks. *Remote Sensing of Environment*, *114*, 183–198.

Huang, C., & Townshend, J. R. G. (2003). A stepwise regression tree for nonlinear approximation: Applications to estimating subpixel land cover. *International Journal of Remote Sensing*, *24*, 75–90.

Kassawmar, N. T., Rao, K. R. M., & Abraha, G. L. (2011). An integrated approach for spatio-temporal variability analysis of wetlands: A case study of Abaya and Chamo lakes, Ethiopia. *Environmental Monitoring and Assessment*, *180*, 313–324.

Klemas, V. V., Dobson, J. E., Ferguson, R. L., & Haddad, K. D. (1993). A coastal land cover classification system for the NOAA coastwatch change analysis project. *Journal of Coastal Research*, *9*, 862–872.

Kramer, H. J. (2002). *Observation of the earth and its environment: Survey of missions and sensors*. Berlin: Springer, 1510.

Kudray, G., & Gale, M. (2000). Evaluation of National Wetland Inventory maps in a heavily forested region in the upper Great Lakes. *Wetlands*, *20*, 581–587.

Lang, M. W., & Kasischke, E. S. (2008). Using C-band synthetic aperture radar data to monitor forested wetland hydrology in Maryland's Coastal Plain, USA. *IEEE Transactions on Geoscience and Remote Sensing*, *46*, 535–546.

Lang, M. W., Kasischke, E. S., Prince, S. D., & Pittman, K. W. (2008). Assessment of C-band synthetic aperture radar data for mapping and monitoring Coastal Plain forested wetlands in the Mid-Atlantic Region, USA. *Remote Sensing of Environment*, *112*, 4120–4130.

Lang, M. W., & McCarty, G. W. (2009). Lidar intensity for improved detection of inundation below the forest canopy. *Wetlands*, *29*, 1166–1178.

Lang, M., McCarty, G., Oesterling, R., & Yeo, I. Y. (2013). Topographic metrics for improved mapping of forested wetlands. *Wetlands*, *33*, 141–155.

Lang, M., McDonough, O., McCarty, G., Oesterling, R., & Wilen, B. (2012). Enhanced detection of wetland-stream connectivity using LiDAR. *Wetlands*, *32*, 461–473.

Lee, J. (1980). Digital image-enhancement and noise filtering by use of local statistics. *IEEE Transactions on Pattern Analysis and Machine Intelligence*, *2*, 165–168.

Li, A., Huang, C., Sun, G., Shi, H., Toney, C., Zhu, Z., et al. (2011). Modeling the growth of young forests regenerating from recent disturbances in Mississippi using Landsat time series observations and ICESat/GLAS lidar data. *Remote Sensing of Environment*, *115*, 1837–1849.

Loveland, T. R., & Dwyer, J. L. (2012). Landsat: Building a strong future. *Remote Sensing of Environment*, *122*, 22–29.

Lu, Z., Crane, M., Kwoun, O. -I., Wells, C., Swarzenski, C., & Rykhus, R. (2005). C-band radar observes water level change in swamp forests. *Eos, Transactions American Geophysical Union*, *86*, 141–144.

Lunetta, R. S., & Balogh, M. E. (1999). Application of multi-temporal Landsat 5 TM imagery for wetland identification. *Photogrammetric Engineering & Remote Sensing*, *65*, 1303–1310.

Markham, B.L., & Helder, D. L. (2012). Forty-year calibrated record of earth-reflected radiance from Landsat: A review. *Remote Sensing of Environment*, *122*, 30–40.

Masek, J. G., Vermote, E. F., Saleous, N. E., Wolfe, R., Hall, F. G., Huemmrich, K. F., et al. (2006). A Landsat surface reflectance dataset for North America, 1990–2000. *IEEE Geoscience and Remote Sensing Letters*, *3*, 68–72.

McCarty, G., McConnell, L., Hapernan, C., Sadeghi, A., Graff, C., Hively, W., et al. (2008). Water quality and conservation practice effects in the Choptank River watershed. *Journal of Soil and Water Conservation*, *63*, 461–474.

Mitsch, W. J., & Gosselink, J. G. (2007). *Wetlands, New York, USA*. New York: John Wiley and Sons.

Moore, J. E., & Kim, T. J. (1995). Mills' urban system models: Perspective and template for LUTE (land use transport environment) applications. *Computers, Environment and Urban Systems*, *19*, 207–225.

Nelson, K. C., & Palmer, M.A. (2007). Stream temperature surges under urbanization and climate change: Data, models, and responses. *Journal of the American Water Resources Association*, *43*, 440–452.

Nestler, J., & Long, K. (1997). Development of hydrological indices to aid cumulative impact analysis of riverine wetlands. *Regulated Rivers-Research & Management*, *13*, 317–334.

Niehoff, D., Fritsch, U., & Bronstert, A. (2002). Land-use impacts on storm-runoff generation: Scenarios of land-use change and simulation of hydrological response in a meso-scale catchment in SW-Germany. *Journal of Hydrology*, *267*, 80–93.

Nielsen, E. M., Prince, S. D., & Koeln, G. T. (2008). Wetland change mapping for the US mid-Atlantic region using an outlier detection technique. *Remote Sensing of Environment*, *112*, 4061–4074.

Ozesmi, S., & Bauer, M. (2002). Satellite remote sensing of wetlands. *Wetlands Ecology and Management*, *10*, 381–402.

Powell, S. L., Cohen, W. B., Healey, S. P., Kennedy, R. E., Moisen, G. G., Pierce, K. B., et al. (2010). Quantification of live aboveground forest biomass dynamics with Landsat time-series and field inventory data: A comparison of empirical modeling approaches. *Remote Sensing of Environment*, *114*, 1053–1068.

Rogers, A. S., & Kearney, M. S. (2004). Reducing signature variability in unmixing coastal marsh Thematic Mapper scenes using spectral indices. *International Journal of Remote Sensing*, *25*, 2317–2335.

Ruan, R., Feng, X., & She, Y. (2007). Fusion of RADARSAT SAR and ETM + imagery for identification of fresh water wetland. *Proceedings of the SPIE 6752. May 25, 2007, Nanjing, China* (pp. 675221–675231).

Rundquist, D. C., Narumalani, S., & Narayanan, R. M. (2001). A review of wetlands remote sensing and defining new considerations. *Remote Sensing Reviews*, *20*, 207–226.

Schott, J. R. (2007). *Remote sensing: The image chain approach*. Oxford, UK: Oxford University Press.

Stolt, M., & Baker, J. (1995). Evaluation of National Wetland Inventory maps to inventory wetlands in the Southern Blue Ridge of Virginia. *Wetlands*, *15*, 346–353.

Stoner, E. R., & Baumgardner, M. F. (1981). Characteristic variations in reflectance of surface soils. *Soil Science Society of America Journal*, *45*, 1161–1165.

Thomas, R. F., Kingsford, R. T., Lu, Y., & Hunter, S. J. (2011). Landsat mapping of annual inundation (1979–2006) of the Macquarie Marshes in semi-arid Australia. *International Journal of Remote Sensing*, *32*, 4545–4569.

Tiner, R. W. (1999). *Wetland indicators: A guide to wetland identification, delineation, classification, and mapping*. Washington DC, USA: Lewis Publishers.

Tucker, C. J. (1979). Red and photographic infrared linear combinations for monitoring vegetation. *Remote Sensing of Environment*, *8*, 127–150.

Vermote, E. F., ElSaleous, N., Justice, C. O., Kaufman, Y. J., Privette, J. L., Remer, L., et al. (1997). Atmospheric correction of visible to middle-infrared EOS-MODIS data over land surfaces: Background, operational algorithm and validation. *Journal of Geophysical Research-Atmospheres*, *102*, 17131–17141.

Walker, W. S., Kellndorfer, J. M., LaPoint, E., Hoppus, M., & Westfall, J. (2007). An empirical InSAR-optical fusion approach to mapping vegetation canopy height. *Remote Sensing of Environment*, *109*, 482–499.

Wilen, B. O., & Bates, M. K. (1995). The US Fish and Wildlife Service's National Wetlands Inventory Project. In C. M. Finlayson, & A. van der Valk (Eds.), *Classification and inventory of the world's wetlands. Advances in Vegetation Science*, *Vol. 16*. (pp. 153–169). Netherlands: Springer.

Yang, L., Huang, C., Homer, C. G., Wylie, B. K., & Coan, M. J. (2003). An approach for mapping large-area impervious surfaces: Synergistic use of Landsat 7 ETM+ and high spatial resolution imagery. *Canadian Journal of Remote Sensing*, *29*, 230–240.